Statistical Energy Minimization Theory for Systems of Drop-Carrier Particles

Ryan Shijie Du,[1] Lily Liu,[2] Simon Ng,[3] Sneha Sambandam,[1] Bernardo Hernandez Adame,[4] Hansell Perez,[5] Kyung Ha,[1] Claudia Falcon,[1] Joseph de Rutte,[3] Dino Di Carlo,[3,6] and Andrea L. Bertozzi[1,6]

[1] *Department of Mathematics, University of California, Los Angeles*
[2] *Department of Mathematics, University of Chicago*
[3] *Department of Bioengineering, University of California, Los Angeles*
[4] *Department of Mathematics, Massachusetts Institute of Technology*
[5] *Department of Mathematics, University of California, Merced*
[6] *Department of Mechanical Engineering, University of California, Los Angeles*

Drop-Carrier Particles (DCPs) are solid microparticles designed to capture uniform microscale drops of a target solution without using costly microfluidic equipment and techniques. DCPs are useful for automated and high-throughput biological assays and reactions, as well as single cell analyses. Surface energy minimization provides a theoretical prediction for the volume distribution in pairwise droplet splitting, showing good agreement with macro-scale experiments. We develop a probabilistic pairwise interaction model for a system of such DCPs exchanging fluid volume to minimize surface energy. This leads to a theory for the number of pairwise interactions of DCPs needed to reach a uniform volume distribution. Heterogeneous mixtures of DCPs with different sized particles require fewer interactions to reach a minimum energy distribution for the system. We optimize the DCP geometry for minimal required target solution and uniformity in droplet volume.

I. INTRODUCTION

Uniform, fixed volume, microscale fluid droplets are a powerful tool for performing high-throughput bioassays [1, 2] as well as single-cell analyses [3–5]. Traditionally, microfabricated chambers or microfluidic droplet generators are used to create nanoliter-scale compartments to perform these assays [1–3, 5]. A significant downside to these approaches is that they require expensive microfluidic equipment and specialized skills, limiting the adoption of the techniques in most research labs [6]. Recently, Drop-Carrier Particles (DCPs) have emerged as an alternative microparticle-based approach to create uniform compartments for performing biological assays [7–10]. This approach has been used to perform more sensitive molecular assays by accumulating the signal from enzymatic reactions in the small volumes inside the DCPs [7, 9] as well as to probe secreted molecules from single cells, that accumulate at higher concentrations in the nanoliter-scale volumes [7, 8]. DCPs are simple to use, and are compatible with standard readily accessible lab equipment such as microscopes and flow cytometers. This unique capability can enable democratized access to more sensitive tools for fundamental biological discovery, improved diagnostics, and development of antibody and cellular therapies.

DCPs utilize unique geometries and surface tension properties to capture uniform volumes of fluid upon simple mixing within a surrounding immiscible fluid phase. Previous experimental work has demonstrated formation of uniform droplets using DCPs with various shapes, including 3D crescents, hollow cylinders (FIG. 1), and C-shaped DCPs [7]. In general, the DCPs are comprised of (1) a partially exposed inner cavity made from a hydrophilic material that captures a uniform volume of target fluid (e.g. water) and (2) a hydrophobic outer layer

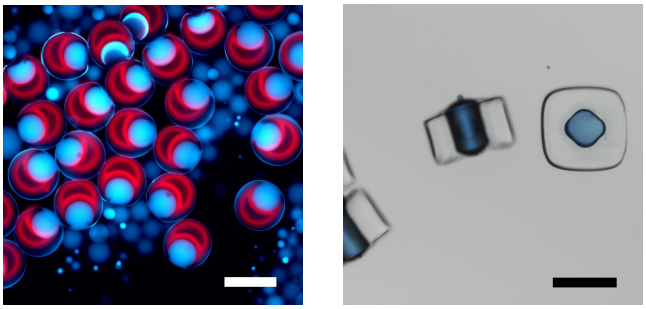

(a) (b)

FIG. 1. Examples of microscopic Drop-Carrier Particles (DCPs) [8, 9]. (a) Spherical crescent-shaped DCPs (red) encapsulating an aqueous phase (blue) in oil phase (black). Scale 100 μm. (b) Hollow cylindrical DCPs (outlined black) encapsulating an aqueous phase (blue) on side and top view. Scale 300 μm.

that preferentially wets the immiscible surrounding fluid (e.g. oil) and protects the captured fluid volume. DCPs are suspended in oil and an aqueous target solution that may contain samples of interest such as cells, proteins or other biological entities. Mixing the system causes DCPs to collide, resulting in redistribution of the captured aqueous solution between the DCP cavities until an equilibrium condition is reached in the system or mixing is stopped.

DCPs are sufficiently small so that surface tension dominates the equilibrium physics (see TABLE I). We use the theory of minimal surfaces with volume constraints [11–14] to study the equilibrium configurations for a variety of fixed volumes and DCPs shapes and sizes. Recently, the authors of [7] developed a fully 3D model that can be applied to arbitrarily-shaped DCPs. However, this model is computationally demanding. The au-

thors of [15] consider axisymmetric DCP geometries, using crescent and cylindrical DCPs as examples. With a foundational understanding of how the surface energy of a single DCP varies with encapsulated fluid volume, they introduce a pairwise interaction model for a system of DCPs. Their theory shows that for sufficiently large volumes of fluid, the minimal energy configuration results in each DCP containing uniform sized droplets. Our work is complementary.

In this paper, we numerically model two DCP geometries, axisymmetric crescents and hollow cylinders as seen in FIG. 2(a) and FIG. 2(b). In Section II, we investigate the fluid-filling behavior of single DCPs, followed in Section III by a study of interactions between two DCPs, which is validated with physical macro-scale experiments. We extend the two-DCP study to include interactions between two different (heterogeneous) sized DCPs. In Section IV, we build upon the two-DCP model to explore multi-DCP systems that are either homogeneous or heterogeneous. We use a mixture model [16] to derive the probability density function (PDF) for the number of Independent Random Interactions (IRIs) required for all DCPs to contain a uniform volume of target solution. Finally, in Section V, we present a parametric study of DCP geometries searching for an optimal DCP for applications.

II. MINIMUM ENERGY THEORY FOR AN AXISYMMETRIC PARTICLE

In this section, we review the minimal energy theory to model the behavior of a target fluid captured by single axisymmetric DCP. We focus on the crescent and hollow cylindrical DCPs as shown in FIG. 2(a) and FIG. 2(b), and we take the target fluid to be water and the surrounding fluid to be oil.

We determine the equilibrium configuration for a DCP with a specified water volume by solving the corresponding energy minimization problem for surface configurations with volume constraints (FIG. 2(c)) [15]. The surface energy E of a three phase DCP-water-oil system is

$$E = \sigma_{\text{wo}} A_{\text{wo}} + \sigma_{\text{wp}} A_{\text{wp}} + \sigma_{\text{op}} A_{\text{op}} \tag{1}$$

where A_{wo} is the surface area of the water-oil interface, A_{wp} that of the water-DCP interface, and A_{op} that of the oil-DCP interface. σ's correspond to the interfacial energies per area. Our DCPs have surface components that are either hydrophilic or hydrophobic, therefore the corresponding surface energy has additional terms analogous to (1). Our model assumes that the buoyancy effects are negligible, and surface tensions dominate, consistent with on the microscale.

For an axisymmetric DCP, the minimal surface configuration is comprised of partial spheres with a contact angle that satisfies the Young-Dupré equation on smooth surfaces [13, 17]. If the DCP has two openings (e.g.: cylinder), the two spheres share the same radius. This

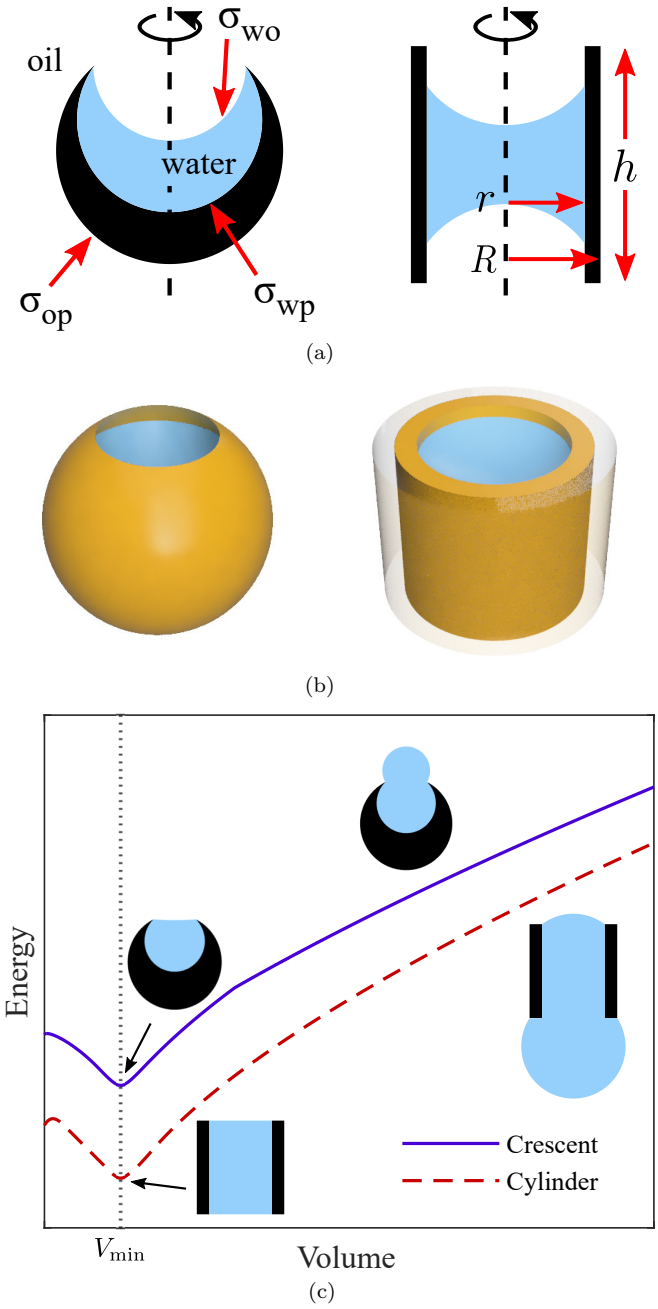

FIG. 2. Basic parameters and behavior of axisymmetric crescent and cylindrical DCPs. (a) Cross section of crescent and cylindrical DCPs. The blue represents the water phase, black the DCP, and white the surrounding oil. The σ's are interfacial energies per area for each interface, and the cylinder is labelled with geometry parameters. (b) The full crescent and cylindrical DCP. The experimental cylinder has two layers, one hydrophilic layer (yellow) and one hydrophobic layer (clear). (c) The corresponding Energy-Volume graph for a cylinder and crescent DCP. The offset between the two curves is artificially added for illustration.

fact reduces the scope of the numerical search for minimal energy configurations. The theoretical properties of the energy-volume $E-V$ graph have been extensively studied in [15]. For example, the energy minimum occurs when the oil-water surface is flat (see FIG. 2(c)). Crescent and cylindrical DCPs can be efficiently fabricated at the micro-scale and are simple to model computationally. The crescent DCPs are introduced in [8, 15]. They are hydrophilic spherical DCPs with a smaller offset sphere removed, creating a fishbowl shape as shown in FIG. 2(a). The crescent geometry has three parameters: the radius of the inner carved-out sphere, the opening aperture, and the outer radius of the DCP. The hollow cylindrical DCPs are introduced in [9]. They are hydrophilic inside and on the ends while the outer surface is hydrophobic. The geometry has three parameters: the inner radius r, the outer radius R, and the height h (see FIG. 2(b)). Though the physical cylindrical DCPs have certain thickness of both the hydrophilic and hydrophobic layers [9] (FIG. 2(b)), the thickness of the hydrophobic layer has minimal effect on the exterior wetting and is neglected in the model.

III. TWO-PARTICLE INTERACTION

In this section we experimentally measure the exchange of fluid between two DCPs and compare the results with theoretical energy minima for a two-DCP system. From the energy volume graph in FIG. 2 one can derive a solution to the energy minimization problem of a two-DCP system

$$\min_{0\leq V\leq V_T} \{E_1(V) + E_2(V_T - V)\} \tag{2}$$

for a fixed total volume V_T. Here the total energy is composed of the energy of the first DCP with volume V, $E_1(V)$, and the energy of the second DCP, $E_2(V_T - V)$. This provides a theoretical prediction to compare with experiments, which we perform on a macro-scale to accurately measure the volume V and $V_T - V$. We use cylindrical DCPs as they are easier to fabricate and sturdier to work on the macro-scale. We conduct experiments on DCPs of equal size and shape as well as experiments with different sizes (FIG. 4). We denote these plots as splitting graphs, where we plot the individual DCP volumes (V and $V_T - V$) against the total volume (V_T).

A. Experimental Methods

To experimentally validate our models, we perform experiments with macro-scale DCPs, which can be individually maniupulated and easily visualized. Macro-scale DCPs are fabricated of the same two polymers used to make micro-scale DCPs, hydrophilic poly(ethylene glycol) diacrylate (PEGDA, Mw $\approx$ 575; 437441, Sigma-Aldrich) and hydrophobic poly(propylene glycol) diacrylate (PPGDA, Mw $\approx$ 800; 455024, Sigma-Aldrich). Both polymers are mixed with 1% V:V photoinitiator (2-hydroxy-2-methylpropiophenone, Darocur 1173, 405655, Sigma-Aldrich) for UV-crosslinking. We fabricate macro-scale DCPs with an inner hydrophilic layer (PEGDA) and outer hydrophobic layer (PPGDA) as previously described [7]. Using this approach we are able to create macro-scale DCPs with minimal variation in size and shape (CV<10%).

To replicate the physics of the microscale system with the macro-scale DCP's we use hydrophilic and hydrophobic fluid phases that have minimal density differences to study fluid break up. This is critical since surface tension forces dominate other forces such as gravity at the microscale (i.e. Bond number $<<$ 1). For the outer hydrophobic fluid phase we use uncrosslinked, liquid PPGDA as it has similar density to water (1.07 g/cm^3). To minimize the gravitational effects further, we adjust the density of the water phase to match PPGDA by adding 8% V:V glycerol to the water solution, which results in a small Bond number (TABLE I).

We experimentally study the splitting behavior of two DCPs using a 3D-printed, motorized rig in which macro-DCPs are clamped to and pulled apart at a constant speed while submerged in PPGDA oil (see FIG. 3(a)). We begin the experiment with the DCPs touching and their aqueous fluid distributed between the DCPs as seen at $t = 0$ s in FIG. 3(b). We then pull the DCPs apart at a relative speed of about 1 mm/s from each other. This is slow enough that dynamic effects are limited (TABLE I). Eventually, the catenoid formed between the DCPs breaks, at which point we stop the experiment and carefully remove the DCPs from the PPGDA oil bath, leaving behind the water droplets captured by each DCPs as a sphere. We take a top view image of the water droplets and process the photos in MATLAB to calculate the volume of the water in each DCPs. We compare these observations with our simulations in FIG. 4.

Additionally, we match our simulation's surface tension coefficients to the macro-scale experiments by making contact angle measurements. First, we normalize the water-oil coefficient $\sigma_{\text{wo}} = 1$. From here, we only need to examine the energy deviations from the empty DCP energy. Thus, we are only interested in $\sigma_{\text{op}} - \sigma_{\text{wp}}$, which is given by the contact angle [13]. We measure the contact angle of a water droplet on a flat hydrophilic slab with the droplet and slab submerged in oil. The contact angle is 69.5°, so $\sigma_{\text{op}} - \sigma_{\text{wp}} = \cos(69.5°) = 0.35$.

B. Homogeneous Interaction

We study the interaction between a pair of homogeneous DCPs with the same shape and same size. Theoretical prediction of the behavior of the particle splitting graph can be found in [15]. In particular, authors of [15] prove that there exists a volume V_1 such that for all volume $V_T < V_1$, one DCP takes no volume. They also prove that there exists a volume V_b such that for all vol-

	Reynolds Number	Bond Number	Ohnesorge Number	Weber Number	Capillary Number
Expression	$\rho u L/\mu$	$\Delta\rho g L^2/\sigma$	$\mu/\sqrt{\rho\sigma L}$	$\rho u^2 L/\sigma$	$\mu u/\sigma$
Experiments in [10]	2×10^{0}	1×10^{-4}	3×10^{0}	2×10^{1}	1×10^{1}
Experiments in Section III	4×10^{-2}	4×10^{-2}	4×10^{-1}	3×10^{-4}	6×10^{-3}

TABLE I. Dimensionless number estimates. ρ, u, L, μ, g and σ are the density, characteristic velocity, characteristic length, viscosity, gravitational acceleration, and surface tensions respectively.

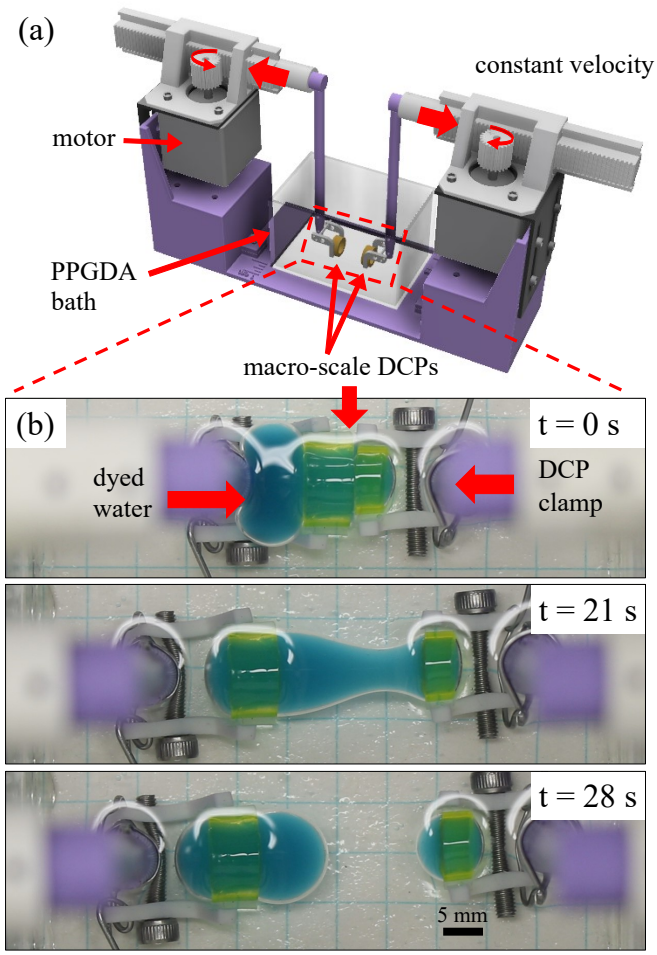

FIG. 3. Experimental setup and time-lapse of macroscopic two-DCP interaction. (a) CAD diagram illustrating the experimental setup for making two DCPs interact by pulling them apart. (b) Top-view of time-lapse experiment of heterogeneous cylindrical DCPs (yellow) which are filled with a water-glycerol mixture (blue), submerged in a PPGDA bath. The left DCP is approximately twice the dimensions of the smaller right DCP. Scale 5 mm. Graph pad squares 6.35 mm.

ume $V_T \geq 2V_b$, one DCP takes volume in a specific range around $V_{\min}$ and the other DCP takes the rest.

The splitting graph of two identical cylinders is shown in FIG. 4(a), with the experimental data overlaid. The experimental macro-scale cylinders have an inner radius $r = 2.8$ mm, a hydrophilic layer radius $R = 4.0$ mm, a hydrophobic layer radius $R_{hb} = 5.2$ mm, and a height $h = 8$ mm. The physical system exhibits the same important splitting properties. For a range of small total volumes (V_T), one DCP takes no water. We call this interval the No-Splitting Range. There is another interval of V_T where DCPs split the volume evenly, called the Even-Splitting Range. For large V_T, one DCP takes close to its energy minimizing volume $V_{\min}$ while the other DCP takes the remaining water. This is called the Large-Volume-Limit Range. For a labelled example splitting graph, see FIG. 5(a), and for the precise definitions, see Section IV.

C. Heterogeneous Interactions

In this section, we explore the splitting of different sized DCPs of the same shape, which we call a heterogeneous interaction. Heterogeneous interactions take place between a small and a large DCP of the same shape. These interactions can optimize mixing (discussed in Section IV B). Here we consider a case study with a large cylinder ($r = 5.0$ mm, $R = 6.0$ mm, $R_{hb} = 7.0$ mm, and $h = 6.0$ mm) and a small cylinder ($r = 2.8$ mm, $R = 4.0$ mm, $R_{hb} = 5.2$ mm, and $h = 3.0$ mm). The splitting graph of both experimental results and theoretical results for these heterogeneous DCPs are shown in FIG. 4(b). Unlike homogeneous DCP interactions in FIG. 4(a), heterogeneous interactions lack an Even-Splitting Range (i.e. water does not evenly distribute between particles), which we exploit in our theory. Otherwise, the heterogeneous system exhibits a similar behavior as the homogeneous system with the No-Splitting Range for small V_T and the Large-Volume-Limit Range for large V_T.

In the No-Splitting Range, experimental results match well with theory; in the Large-Volume-Limit Range, there is a discrepancy between experiments and the theoretical volumes that minimize (2). This discrepancy is explained by the difference between the global and local energy minimizers as well as system dynamics. One volume configuration minimizing (2) is the global energy minimizer, in which the small DCP has zero water volume and the large DCP has all of the water. However, both DCPs take water volume in a manner more consistent with the local energy minimizer of (2), in which the small DCP takes a volume close to the single DCP energy minimizing volume ($V_{\min}$) and the large DCP takes the remaining water. The preference towards the local energy minimizer is due to the energy associated with dewetting a DCP. Additionally, for *admissible* DCPs that are defined and studied in Section IV, the local non-zero min-

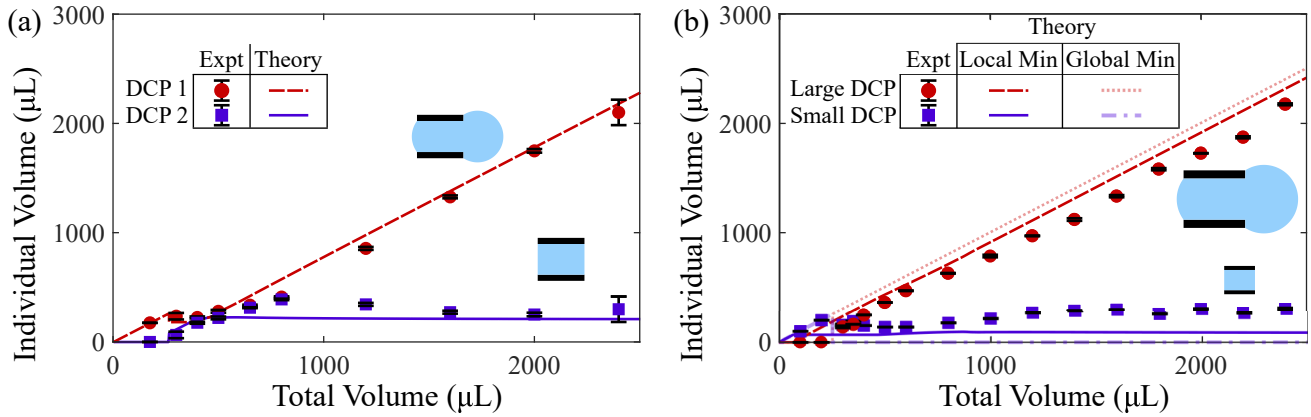

FIG. 4. Fluid splitting graphs for cylindrical DCPs: (a) Splitting graph for two identical cylindrical DCPs (b) Splitting graph for two heterogeneous cylindrical DCPs, where one cylinder is larger than the other. The measurements of physical experiments (Expt) and the theoretical predictions based on the discussions of section III and [15] (Theory) are respectively represented by dots with error bars and colored lines. Experimental data (each point represents 3 trials and the error bars are one standard deviation long) is compared to theoretical results with particle geometry and surface tensions that match the physical experiment, explained in Section III A.

imizer is in fact the global minimizer. FIG. 4(b) shows that the local energy minimizer explains the experimental data better than the global energy minimizer. However, the local energy minimizer still does not completely explain experimental observations, but there is a fairly uniform volume difference between the two. This is due to the dynamics of capillary breakup, which we do not consider in our theoretical predictions. [18]. For simplicity, we continue using the tractable energy minimizing strategy from (2) in our subsequent sections as an approximation of pairwise water splitting behavior.

IV. SYSTEMS OF MULTIPLE PARTICLES

In this section, we use the pairwise splitting model to simulate multi-DCP systems (homogeneous and heterogeneous). Within a system of DCPs, the DCPs exchange fluid with each other in randomly-chosen, pairwise interactions – resembling how DCPs collide and exchange fluids in experiments – to achieve a system-wide minimal energy distribution, resulting in a uniform distribution of water among the DCPs. These pairwise interactions follow the two-DCP splitting graph (FIG. 4).

We develop an analytic theory for the PDF of the number of these Independent Random Interactions (IRIs) required for homogeneous and heterogeneous systems to converge to equilibrium and show that the theory agrees well with numerical simulations. We further investigate the effects of heterogeneous DCPs on the number of IRIs. As long as the DCPs satisfy our requirements for α-*admissible* DCPs, as defined in Section IV B, this new theory is independent of the DCP geometry.

A. Number of Independent Random Interactions for Homogeneous Systems

We first study the number of IRIs for a system of homogeneous DCPs, i.e. identical DCPs. We initialize the homogeneous system with all the water in one DCP. The system has converged when all but one DCPs contain water volume around $V_{\min}$, the energy minimizing volume, and the remaining DCP contains the excess water volume.

In Section III B, we introduce three volume ranges (FIG. 5(a)). Here we also name their end points.

A: No-Splitting Range: the interval, $[0, W_{A,U}]$, of small total volumes (V_T) where one DCP takes no water

B: Even-Splitting Range: the interval $[W_{B,L}, W_{B,U}]$ of V_T where the DCPs split water evenly

C: Large-Volume-Limit Range: the interval $[W_{C,L}, \infty)$ of V_T where one DCP is filled, i.e. contains a volume in $[F_L, F_U]$, while the other DCP takes the remaining water. We define $F_L = \frac{W_{B,L}}{2}$ (FIG. 2) and $F_U = \min\left(W_{A,U}, \frac{W_{B,U}}{2}\right)$.

We show shortly that these are the only possible volumes, the other volumes are therefore not considered. After two DCPs interact, we denote the resulting smaller volume V_{sm} and the larger volume V_{lg}. To consider a system with simple DCP interaction behavior, we introduce the concept of an *admissible* DCP. We define a DCP to be an *admissible* DCP if

$$F_L \leq V_{\min} < F_U.$$

All crescent and cylinder DCPs studied in this paper are *admissible* DCPs.

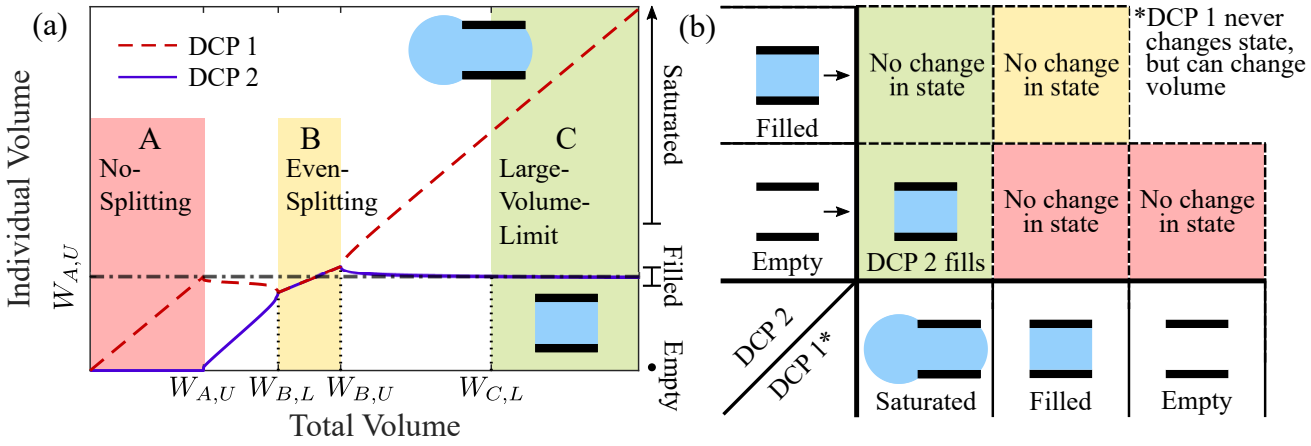

FIG. 5. (a) An illustrative example of a homogeneous fluid splitting graph. $W_{A,U}$, $W_{B,L}$, $W_{B,U}$, and $W_{C,L}$ represent upper or lower volume boundaries of the No-Splitting (A), Even-Splitting (B), and Large-Volume-Limit (C) Ranges which are important to our analysis. $V_{\min}$ is the energy minimizing volume for a single DCP and is represented in FIG. 2. (b) Possible DCP-DCP interactions in homogeneous system. DCPs can be in one of three states - empty, full, or saturated, carrying the entire system's excess fluid. Each dashed box indicates the equilibrium state after a 2-DCP interaction. The background color corresponds with a splitting range in (a), based on the summed volume of the initial DCPs.

We now consider a system of $N+1$ *admissible* DCPs. The system initially has all the of water attached to one DCP with the remaining DCPs empty. When the total system volume V_{t0} satisfies

$$V_{t0} \geq W_{C,L} + (N-1) \cdot F_U, \tag{3}$$

we claim that throughout the entire mixing process there are only three possible DCP states - empty DCPs, filled DCPs, and one saturated DCP with the remaining volume. A change in state would be, for example, an empty DCP becoming filled after interacting with the saturated DCP. We show this by considering all the possible interactions in a system as described above, which is summarized in FIG. 5(b). For any pairwise interaction, we know that if $V_T > W_{C,L}$, one DCP is filled and the other DCP contains the remaining volume. Since $V_{t0} > W_{C,L}$, an interaction between the initial saturated DCP and an empty DCP results in one filled DCP and one saturated DCP. This is still the case for all subsequent interactions between empty DCPs and the saturated DCP because the volume in the saturated DCP satisfies $V_{t0} - iW_{A,U} > W_{C,L}$ for all $i \in \{0, 1, \ldots, N-1\}$, the number of filled DCPs. The same reasoning shows that the interaction between a saturated DCP and a filled DCP does not result in any state change. Also since there is no interaction that results in two saturated DCPs, there is only one saturated DCP throughout the model. When two filled DCPs interact, the total system volume satisfies $W_{B,L} \leq 2F_U \leq W_{B,U}$, which results in even splitting. Although the volume in each DCP may change, both DCPs remain in the filled state. When a filled DCP interacts with an empty DCP, the total system volume is at most $W_{A,U}$. By the definition of $W_{A,U}$, we know that this interaction leaves one DCP empty, thus not changing the states of either DCP. It is clear that two empty DCPs do not change states after interaction. We have therefore showed that throughout the mixing process, all DCPs will fall into one of the three DCP states.

For the homogeneous system of DCPs, *convergence* is defined to be when all DCPs are filled except for the saturated DCP. The number of IRIs is defined as the number of pairwise random interactions to reach system *convergence*. The only state change occurs when an empty DCP becomes filled. Since filled DCPs cannot become empty, the number of filled DCPs monotonically increases and eventually every DCP except the saturated one becomes filled. The system reaches *convergence* in a finite number of interactions with probability one.

For a system of *admissible* DCPs with a V_{t0} that satisfies (3), the Total Number of IRIs is a random variable that follows a summed geometric distribution:

$$\begin{aligned} &\text{Total Number of IRIs} = \sum_{i=0}^{N-1} X_i, \\ &\text{where } X_i \sim \text{Geo}(p_i) \text{ with } p_i = \frac{N-i}{\binom{N+1}{2}}. \end{aligned} \tag{4}$$

X_i denotes the number of IRIs until the system makes a successful change of state from i filled DCPs to $(i+1)$ filled DCPs. A system with i filled and $N-i$ empty DCPs has $N-i$ possible pairs (empty-saturated) that can change state out of the total $\binom{N+1}{2}$ possible interactions. Thus the number of IRIs until the next change of state, X_i, is a geometric distribution with the probability parameter p_i. This reasoning is similar to the Coupon Collector's Problem [19]. We validate this theoretical result with numerical simulations in Section IV C.

B. Number of Independent Random Interactions for Heterogeneous Systems

We consider a system of two differently-sized DCPs with the goal of filling all the smaller DCPs. We show that introducing large DCPs into the system decreases the number of IRIs. The system reaches *convergence* when all the small DCPs contain water within some volume range around $V_{\min}$. Here the large DCPs are auxiliary DCPs, providing a mechanism to transfer fluid to the smaller DCPs.

In the heterogeneous system, there are initially N_L large empty DCPs, N_S small empty DCPs, and one saturated large DCP which contains all the initial system volume. A large DCP has the same aspect ratio as a small DCP. And α is the ratio of the length scales of the two DCPs sizes. We assume the DCPs are all *admissible* DCPs, so the results in Section IV A still hold.

In contrast to Section IV A, we only discuss two volume ranges present in FIG. 6(a).

A: No-Splitting Range: small total volumes (V_T) in the range $[W'_{A,L}, W'_{A,U}]$ where one DCP takes no water.

C: Large-Volume-Limit Range: the interval $[W'_{C,L}, \infty)$ of V_T where the small DCP is filled, i.e. contains a volume in $[F'_L, F'_U]$, while the large DCP takes the remaining water. We define $F'_L = \max\{F_L, W'_{A,L}\}$ and $F'_U = \min\{W'_{A,U}, F_U\}$. $[F'_L, F'_U]$ is a subset of $[F_L, F_U]$.

The filled large DCPs contains a volume that is a scaling of the filled volumes of small DCPs as $[\alpha^3 F'_L, \alpha^3 F'_U]$.

Finally, we define an α-*admissible* DCP:

1. Interactions between two same sized α-*admissible* DCPs satisfy the properties of an *admissible* DCP, and
2. Interactions between one small and one large (scale α) DCP have $V_{\min} < W'_{A,U}$.
3. Sufficiently large α (details discussed in Appendix A)

With an $\alpha = 5$, the cylinder and crescent DCPs in the parametric study in Section V are α-*admissible* DCPs. However this is not true in general. For example, short cylinders, with $1 \le h/r < 2$, are not α-*admissible* DCP even though they are *admissible* DCPs.

For a system of α-*admissible* DCPs with total system volume

$$\begin{aligned} V'_{t0} \ge & (N_S - 1) \cdot F'_U + W'_{C,L} + \\ & (N_L - 1) \cdot \alpha^3 F_U + \alpha^3 W_{C,L} \\ =: & V_R \end{aligned} \tag{5}$$

and α sufficiently large (Appendix A), the states of the DCPs are limited to: saturated large, filled large, empty large, filled small, and empty small. We denote this threshold system volume V_R. To show this, we first note that interactions between same-sized DCPs follow the splitting graph from Section IV A. We then investigate interactions between large and small DCPs. When a large filled DCP interacts with a small empty DCP, if α is large enough (Appendix A), the total interaction volume is $V_T \ge \alpha^3 F_L \ge W'_{C,L}$. Thus, the small DCP takes a volume of water that is in the Large-Volume-Limit Range, near $V_{\min}$. Though the large DCP volume decreases slightly, it remains in the Large-Volume-Limit Range. The same reasoning shows that an interaction be-

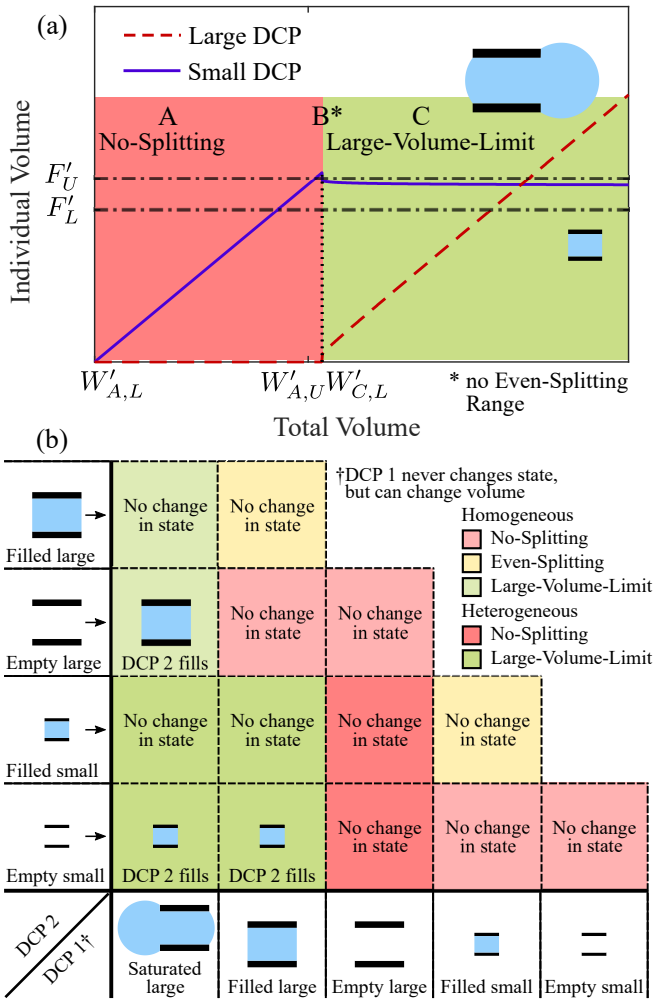

FIG. 6. (a) An illustrative example of a heterogeneous splitting graph. $W'_{A,L}, W'_{A,U}$, and $W'_{C,L}$ represent the lower or upper boundaries of the No-Splitting (A) and Large-Volume-Limit (C) Ranges. For this example, the difference between $W'_{A,U}$ and $W'_{C,L}$ is very small (cf. FIG. 4). Unlike the illustrative example, $W'_{A,L}$ does not necessarily have to be 0. (b) Possible DCP-DCP interactions in the heterogeneous system. The small DCP can be in one of two states - empty or full and the large DCP can be in one of three states - empty, full, or saturated, carrying the entire system's excess fluid. Each dashed box indicates the equilibrium state after a 2-DCP interaction, based on the summed volume of interacting DCPs.

tween a saturated large DCP and a empty small DCP fills the small DCP. For the same reason, (saturated large) − (filled small) and (filled large) − (filled small) interactions do not change the states of the DCPs. Interactions between an empty large DCP and a filled small DCP do not change the states of the DCPs either. The small DCP takes all the volume in the system because the total volume $W'_{A,L} \leq F'_L < V_T < F'_U \leq W'_{A,U}$. Therefore we have shown that for heterogeneous DCP system, there are only three possible interactions that change the states of DCPs. The possible interactions are shown in FIG. 6(b).

Similar to the homogeneous system, the number of IRIs for heterogeneous systems can be calculated theoretically. For a system as described above, the number of filled large and small DCPs monotonically increases, and eventually all small DCPs become filled. At this point, the system has reached *convergence*. The number of IRIs follows a "mixture model" of a summed geometric distribution [16]. Using the mixture model, the calculation of the probability density function generalizes the calculation in Section IV A. A more detailed explanation can be found in Appendix B. This probabilistic methodology is applicable to systems with relaxed assumptions and more states. We validate this theoretical result with numerical simulations in the following section.

C. Probability Density Function Analysis of the number of IRIs

Equation (4) provides the probability density function for the number of IRIs needed to achieve a steady state redistribution of water amongst a large number of homogeneous DCPs. In Appendix B, we present a recurrence procedure for the heterogeneous case of two DCP sizes. Here we compare these theoretical results with numerical simulations of pairwise IRIs. From these results, we find the optimal large to small particle ratio in the heterogeneous system to minimize the number of IRIs needed to reach steady state.

We consider a homogeneous system with 300 DCPs and initial system volume, V_{t0}, satisfying (3). We run 1,000 trials for this system. FIG. 7(a) compares the IRIs distribution of the numerical simulations and our theoretically calculated probability density function (4). We perform a similar comparison of the IRIs distribution for a heterogeneous system with 106 large ($\alpha = 5$) DCPs and 300 small DCPs; all DCPs are empty initially, except for a large DCP that contains V'_{t0} satisfying (5). The results are shown in FIG. 7(b).

From FIG. 7(a) and FIG. 7(b), we observe that introducing large DCPs decreases the number of IRIs required to reach equilibrium, as the presence of filled large DCPs increases the probability that a small DCP becomes filled. However, an excessive number of large DCPs slows the *convergence* of small DCPs. We choose the number of large DCPs to optimize $\overline{M}$ and $\overline{M} + 2\sigma_M$, where $\overline{M}$ is the mean number of IRIs and σ_M is its standard deviation.

We explore the optimal ratios of large to small DCPs for various systems in FIG. 8. We consider a system of 300 small DCPs with i large DCPs. FIG. 8(a) shows $\overline{M}$ and $\overline{M} + 2\sigma_M$ as a function of the number of large DCPs, i. The case with 106 large DCPs minimizes $\overline{M}$ and 113 minimizes $\overline{M} + 2\sigma_M$. Notice that introducing even a few large DCPs decreases the number of IRIs significantly. We repeat this calculation to find the optimal ratio for different numbers of small DCPs (FIG. 8(b)). The ratios that minimize $\overline{M}$ and $\overline{M} + 2\sigma_M$ are between 0.3 and 0.4.

V. OPTIMIZING PARTICLE GEOMETRY

In this section, we present a method to optimize heterogeneous α-*admissible* DCPs to address system uniformity and conservation of target fluid. We first describe the parameters involved and then provide an example of the optimization process for cylindrical DCPs. An optimal DCP shape should minimize the variation of the fluid volume captured by the small DCPs. We consider a heterogeneous system with a sufficiently large initial system volume. After *convergence*, a small DCP is filled.

We define the range size R_C as the possible volume range of water after *convergence*. We calculate R_C numerically by finding the range of volume that the small particle takes in the Large-Volume-Limit Range. This is a subset of the theoretical range $[F'_L, F'_U]$. Moreover, in order to conserve target fluid, the optimal DCP should minimize the threshold system volume V_R. Recall that, in (5), V_R depends on both system parameters and DCP geometry. System parameters include the number of small and large DCPs in a system (N_S and N_L). DCP geometry affects the threshold volumes ($W_{C,L}$ and $W'_{C,L}$) and the upper bound of the filled range (F_U and F'_U). To find an optimal DCP geometry, we fix the system parameters and minimize R_C and V_R by exploring the geometric parameters.

Based on the above criteria, we perform a parametric study on cylinder DCPs to find the best cylindrical geometry for laboratory applications (for crescent geometries see Appendix C). This analysis exemplifies the general procedure of finding optimal DCP geometries within a class of DCPs. Following our discussion of cylinder DCPs in Section II, we view the DCP as hydrophilic with an infinitesimally thin hydrophobic coating on the outside. For our case study, σ_{wo} is normalized to 1. For the hydrophilic surface, the water contact angle is acute with $\cos(\theta) = \sigma_{\text{os}} - \sigma_{\text{ws}} = 0.8$; for the hydrophobic surface, the water contact angle is obtuse with $\cos(\theta) = \sigma_{\text{os}} - \sigma_{\text{ws}} = -0.8$. Additionally, the size ratio of large to small DCP is $\alpha = 5$. We also normalize DCP size such that $V_{\min} = 1$. The cylinder DCP geometries therefore have two parameters: the ratio of outer to inner radius R/r and the ratio of height to inner radius h/r. We vary those two to produce different DCP geometries.

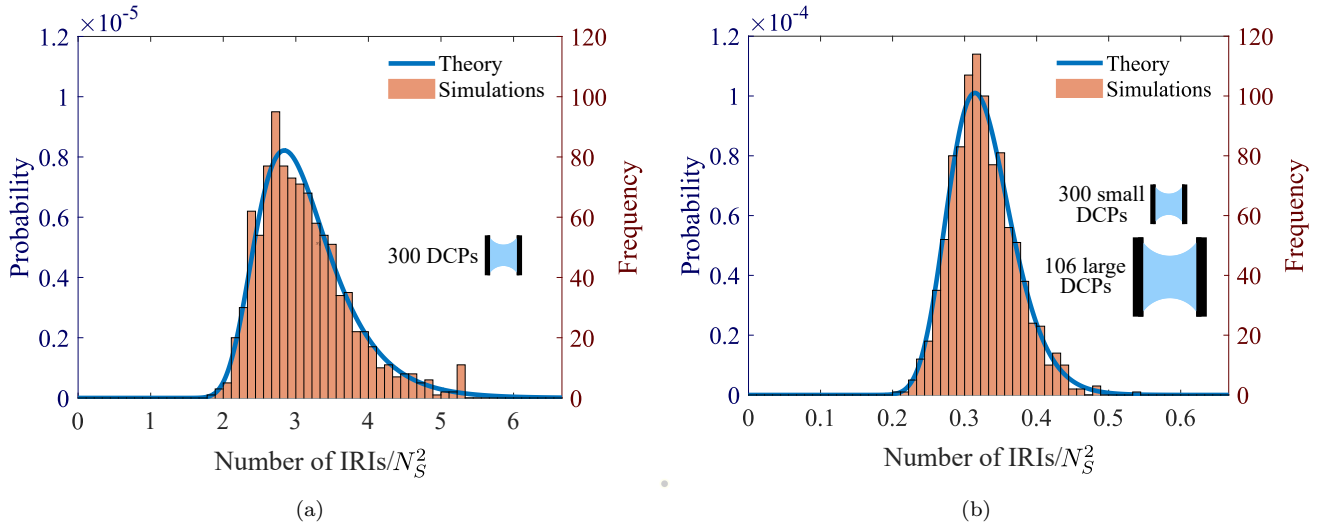

FIG. 7. Theoretical number of IRIs compared with numerical simulations. The histogram shows the distribution of number of IRIs from the numerical simulations (1,000 trials), and the blue curve is our theoretical prediction (4). Notice the change in the range of the x-axis. (a) Number of IRIs of a system with 300 homogeneous DCPs. The system starts with one saturated DCP with sufficiently large volume. (b) Number of IRIs of a system with 106 large DCPs and 300 small DCPs. The system starts with one saturated large DCP with sufficiently large volume.

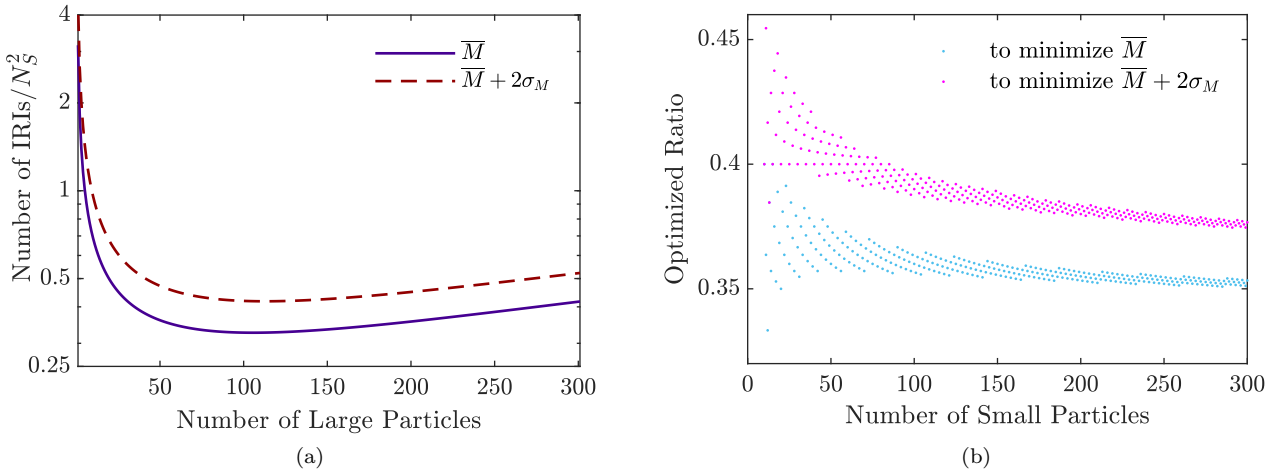

FIG. 8. Optimal number of large DCPs in heterogeneous systems. (a) Number of IRIs needed to achieve steady state vs. the number of large DCPs present. We plot the mean of number of IRIs ($\overline{M}$) and the mean plus two standard deviation of the number of IRIs ($\overline{M}+2\sigma_M$) for a system with 300 small DCPs and varying number of large DCPs. 106 large DCPs minimize $\overline{M}$ and 113 large DCPs minimize the $\overline{M}+2\sigma_M$. The y-axis is on log scale to emphasize the details at small value. (b) The optimal ratio of large to small DCPs to reduce the mean of number of IRIs ($\overline{M}$) or the mean plus two standard deviations of the number of IRIs ($\overline{M}+2\sigma_M$) for different numbers of small DCPs. The optimal ratios for optimizing both are between 0.3 to 0.4. The sweeping pattern is solely a product of the discrete increase in small DCPs.

We find that the optimal cylinder to minimize R_C is long (i.e. has larger h/r). In FIG. 9(a), we present the range of R_C for these geometries. We also see that the outer radius of the DCP does not affect R_C.

To minimize V_R in our parametric sweep, we must choose specific numbers of small and large DCPs. We choose $N_S = 300$ small and $N_L = 106$ DCPs based on Section IV B. We calculate V_R using (5) and present the results in FIG. 9(b). Cylinders that are longer and have a thinner outer wall have lower V_R.

For our example of 300 small and 106 large DCPs, the cylinder DCP that minimizes both R_C and V_R is the DCP that is long and has a thin hydrophilic wall. In FIG. 9(c), we present the 2 dimensional cross section of the optimal cylinder DCP, which has $R/r = 1.1$, and $h/r = 4$. A DCP with such thin walls is structurally unstable. However, the hydrophobic wall thickness does not affect the behavior of the DCP, so the optimal DCP

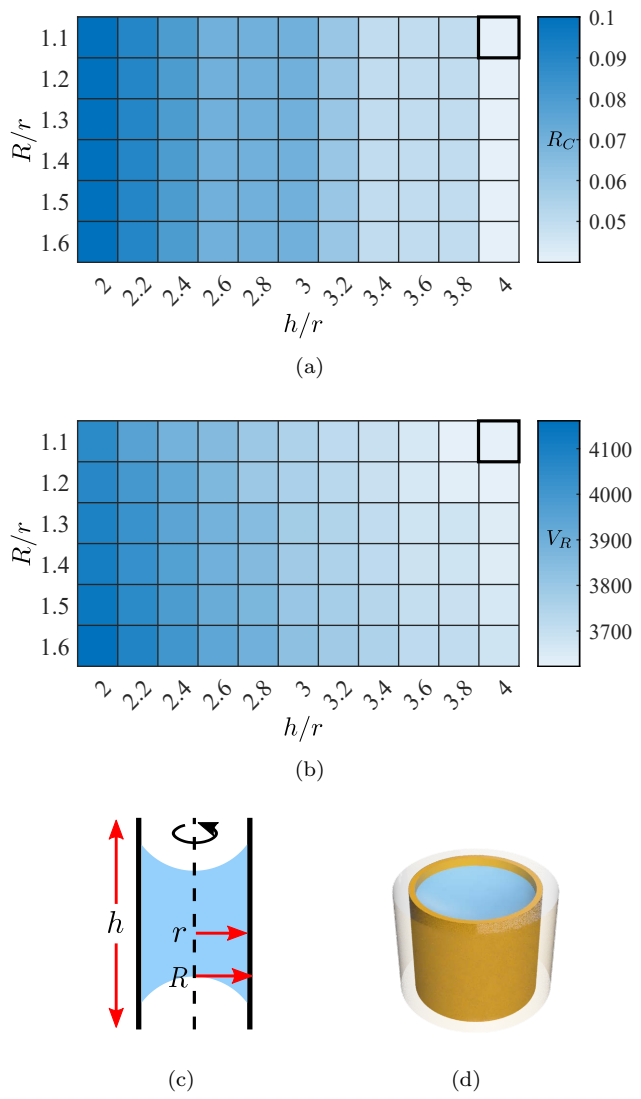

FIG. 9. Parametric sweep of cylinder geometries for DCP optimization. (a) Heat map representing convergent range R_C. (b) Heat map representing initial volume requirement for target fluid V_R. (c) Cross section of optimal cylindrical DCP with outer radius/inner radius $R/s = 1.1$ and height/inner radius $h/r = 4$. This DCP has $R_C = 0.04$ and $V_R = 3623$. (d) Full optimal cylindrical DCP.

can be reinforced with a thick outer hydrophobic layer.

From 9(a), (b), R_C and V_R are dominated by the parameter h/r: R_C and V_R are smaller when h/r is larger. This trend is due to the strong influence of h/r to the relative volume of the partial spheres that bulge outside the cylinder (as the one in FIG. 2(c)) compared to the energy minimizing volume $V_{\min}$. As we increase the h/r ratio, the relative volume of water in the partial spheres decreases, which in turn decreases the values of R_C and V_R.

VI. CONCLUSION

Our study of DCPs provides some theoretical infrastructure for the design of lab-on-a-particle technologies. To better understand these systems, we consider the minimal surface for individual DCPs and develop a theory for homogeneous and heterogeneous DCP interactions and compare with physical experiments in the two-DCP case. Using the theory, we studied many-DCP interactions with the goal of reducing the number of IRIs and determining the optimal DCP shape. Unlike previous studies [7, 8, 15] which only consider monodisperse collections of DCPs, we consider a bidisperse system with two DCP sizes. These heterogeneous systems do not have an Even-Splitting Range (FIG. 4), thus significantly reducing the necessary number of IRIs compared to homogeneous systems. Using our IRIs theory, we optimize DCP geometry for hollow cylinders and crescents. However, additional features need to be considered, such as fragility of the DCPs due to thin wall structures.

Our IRIs theory is the first step to understanding the amount of agitations needed to reach a uniform distribution in applications. Notice that the mixing time is not expected to be proportional to the required number of IRIs. However, with the same total number of DCPs, an appropriate ratio of large DCPs will reduce the number of agitations required. Our fluid exchange experiments were conducted on a slow timescale. Agitated mixtures will have a higher Reynolds number, and particles may come into contact in oblique ways not studied in the present experimental design. This could be explored in future experiments.

ACKNOWLEDGMENTS

This research is supported by NSF grant DMS-1659676, National Science Foundation Grant 1648451, and Simons Math + X Investigator Award 510776.

Appendix A: Condition on Scaling Ratio α for Heterogeneous System

For a heterogeneous system, we consider two sizes of DCPs with the same geometry, with the larger DCP rescaled in length by a factor of $\alpha > 1$. This section explains the theoretical requirements on α for the results in Section IV B to hold. We then show that these constraints can, in practice, be relaxed with minimal impact to our results. We require that $\alpha^3 F_L \geq W'_{C,L}$, so that when a filled large DCP interacts with an empty small DCP, the small DCP is filled. We consider the worst case scenario: all N_S small empty DCPs interact with only one large DCP. We still want the last small DCP to be filled after interaction. Therefore, the large DCPs

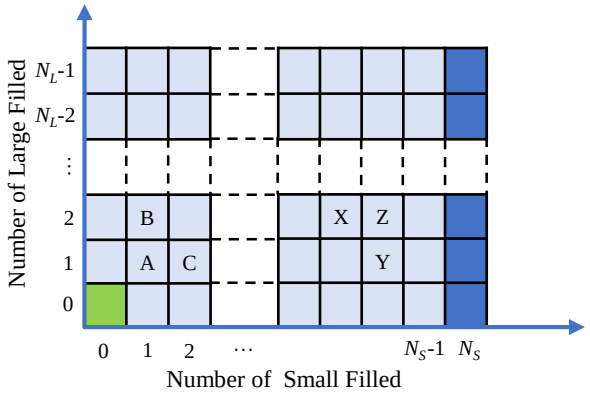

FIG. 10. Graphical representation of all possible states of a heterogeneous DCP system with N_L large DCPs and N_S small DCPs. The green cell represents the initial state with a state array [0 0], and the dark blue cells represent the final states where all small DCPs are filled ($SF = N_S$). The letters in the boxes correspond the three-state systems in FIG. 11.

needs be sufficiently large so that

$$\alpha^3 F_L = \alpha^3 V_{\min} \geq (N_S - 1) \cdot F'_U + W'_{C,L}.$$

If every small DCP transfers volume from one large DCP, the volume in this large DCP should stay within the filled range of the large DCP to ensure that its future interactions follow theoretical predictions. Thus also we need

$$\alpha^3 V_{\min} \geq (N_S - 1) \cdot F'_U + \alpha^3 \frac{W_{B,L}}{2}.$$

These requirements can lead to unreasonably large lower bounds on α, especially in a system with a large number of small DCPs (N_S). However, we can relax the bound on α with minimal deviation from our theory due to the probabilistic nature of the model. The essential condition is that the liquid volume in a filled large DCP should be larger than $W'_{C,L}$ throughout all the interactions. For a reasonable α value and a system with a significant number of large DCPs, there is only a small probability that all the small DCPs interact with a single large one. Additionally, large filled DCPs can interact with the saturated DCP and replenish their volumes.

Appendix B: Proof of Probability Distribution of Number of IRIs

In Section IV B, we show that for a system of large and small α-*admissible* DCPs with a sufficiently large initial volume V'_{t0}, the number of IRIs follows a mixture of summed geometric distributions. This appendix details the calculation for the PDF of the number of IRIs. This calculation is a generalization of the calculation in Section IV A with additional use of the mixture model [16].

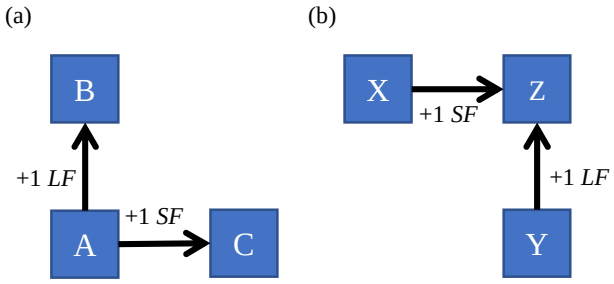

FIG. 11. Graphical representation of example three-state systems. (a) State A can change into State B when a large DCP fills from empty and into State C when a small DCP fills. (b) State Z can be arrived at from State X when a small DCP fills from empty and from State Y when a large DCP fills.

For a system with N_S small particles and N_L large particles, we identify each state of our system in terms of a two element array: [LF SF]. Here, LF is the number of large filled DCPs, and SF is the number of small filled DCPs. The numbers of large empty and small empty DCPs are $N_L - 1 - LF$ and $N_S - SF$ respectively, with one large DCP that stays saturated during the mixing. All the possible states of [LF SF] are organized graphically in FIG. 10.

As we constructed in Section IV B, the heterogeneous system is initialized such that the entire system volume V'_{t0} is in a single large saturated DCP. Therefore, the state array for the initial state is [0 0] and is represented in FIG. 10 as the green cell. As the DCPs interact, there are only three interactions that change the states of the DCPs from empty to filled (FIG. 6). Therefore, LF and SF only increase, which correspond respectively to the state moving upwards or rightwards in FIG. 10. The system reaches *convergence* when $SF = N_S$, which is represented by cells in dark blue in FIG. 10.

Similar to Section IV A, the PDF for the number of interactions needed to fill a DCP (large or small) is modeled as the arrival time of a Bernoulli process. The heterogeneous system is more complicated because there are two possible state changes: a small DCP fills or a large DCP fills. We calculate the number of IRIs needed to reach *convergence* using an inductive argument. The PDF for the number of IRIs needed to move out of a certain state uses information about how a state changes into subsequent states (FIG. 11 (a)). Consider a state A, such that there are two possibilities for the next stage: a large DCP becomes filled and the state moves upward to B or a small DCP becomes filled and the state moves rightward to C. We denote the state arrays: $state_{\mathrm{A}}$= [LF_A SF_A], $state_{\mathrm{B}}$= [$LF_A + 1$ SF_A], and $state_{\mathrm{C}}$= [LF_A $SF_A + 1$].

Given that there are a total of $T = N_S + N_L$ DCPs in the system, the total number of possible interactions is $d = \binom{T}{2}$. The probability that an interaction changes the state of the system from $state_{\mathrm{A}}$ to $state_{\mathrm{B}}$ is denoted p_B. In order for this change of state to happen, one of

the empty large DCPs must become filled by interacting with the saturated DCP, so $p_B = (N_L - 1 - LF_{\mathrm{A}})/d$. Similarly, the probability that an interaction changes the state from $state_{\mathrm{A}}$ to $state_{\mathrm{C}}$ is denoted p_C. For this change of state to occur, one of the small empty DCPs must interact with the saturated large DCP or a filled large DCP, so $p_C = (LF_{\mathrm{A}} + 1)(N_S - SF_{\mathrm{A}})/d$. We consider the process of the system exiting $state_{\mathrm{A}}$ as a Bernoulli process with probability $p_B + p_C$. The PDF for the number of interactions before the state changes from A (to either state B or C) is a geometric distribution:

$$\mathrm{Geo}\left(p_B + p_C\right).$$

We regard the particular jump from $state_{\mathrm{A}}$ to $state_{\mathrm{B}}$ and $state_{\mathrm{A}}$ to $state_{\mathrm{C}}$ as a splitting of the Bernoulli process with the splitting probability $p_B/(p_B + p_C)$ and $p_C/(p_B + p_C)$ respectively [20].

We also need to know the probability that the system visits a certain cell as the system evolves from the initial state to *convergence*. We denote the probability that a path traverses through $state_{\mathrm{A}}$ by q_A and similarly define q_B and q_C for $state_{\mathrm{B}}$ and $state_{\mathrm{C}}$ respectively. We also denote the probability that a path traverses through $state_{\mathrm{A}}$ and then $state_{\mathrm{B}}$ by $q_{A\to B}$; define $q_{A\to C}$ similarly. It is clear that $q_{A\to B} + q_{A\to C} = q_A$. We have from the previous paragraph that

$$q_{A\to B} = q_A \frac{p_B}{p_B + p_C} \quad \text{and} \quad q_{A\to C} = q_A \frac{p_C}{p_B + p_C}.$$

We now change our perspective and focus on how the system reaches a certain state from the two states immediately prior. For example, we single out such a three-state system: a system of three states such that state Z is arrived via state X (from the left) or state Y (from below) (FIG. 11(b)). We describe these states using the state array: $state_{\mathrm{X}}$= $[LF_Z \;\; SF_Z - 1]$, $state_{\mathrm{Y}}$= $[LF_Z - 1 \;\; SF_Z]$, and $state_{\mathrm{Z}}$= $[LF_Z \;\; SF_Z]$.

We observe that $state_{\mathrm{Z}}$ is a mixture of two states described by different PDFs. We assume inductively that we know f_X, f_Y, q_X, and q_Y and use the formula for the theory of mixture models to calculate the mixture's PDF (f_Z) [16] ($*$ denotes convolution):

$$f_Z = r_{X\to Z}(f_X * f_{X\to Z}) + r_{Y\to Z}(f_Y * f_{Y\to Z}), \quad \text{(B1)}$$

where $r_{X\to Z}$ and $r_{Y\to Z}$ are the fraction of $state_{\mathrm{Z}}$ that comes from $state_{\mathrm{X}}$ and $state_{\mathrm{Y}}$ respectively. $f_{X\to Z}$ is the PDF for the number of interactions that occur before the system changes state from $state_{\mathrm{X}}$ to $state_{\mathrm{Z}}$. Then $f_X * f_{X\to Z}$ is the PDF for the number of IRIs needed to reach $state_{\mathrm{Z}}$ from $state_{\mathrm{X}}$ and similarly for $f_Y * f_{Y\to Z}$. Our inductive step is complete if we calculate $r_{X\to Z}$, $r_{Y\to Z}$ and $f_{X\to Z}$, $f_{Y\to Z}$.

From the analysis of the ABC system, we calculate $f_{X\to Z}$, $f_{Y\to Z}$, $q_{X\to Z}$, and $q_{Y\to Z}$. Since all paths that visit $state_{\mathrm{Z}}$ must come from either $state_{\mathrm{X}}$ or $state_{\mathrm{Y}}$, the probability that a path traverses through $state_{\mathrm{Z}}$ is $q_Z = q_{X\to Z} + q_{Y\to Z}$. Then it follows that if a path traverses through $state_{\mathrm{Z}}$, the probability that the path arrives from $state_{\mathrm{X}}$ is

$$r_{X\to Z} = \frac{q_{X\to Z}}{q_Z},$$

and the probability that the path arrives from $state_{\mathrm{Y}}$ is

$$r_{Y\to Z} = \frac{q_{Y\to Z}}{q_Z}.$$

Through this formulation, we now have defined all of the components in (B1) and can calculate the PDF of a new state cell from past state cells. Note that in the edge cases with $SF = 0$ or $LF = 0$, these states have only one source. In addition, the final states have $SF = N_S$ and correspond to the right most column in our state matrix. For these final states, there is only one source, which is from the left, as the cell below has already reached *convergence*.

The final distribution for the number of IRIs is the mixture of these N_L possible end states. For all the possible end states E_i, we have the corresponding probability that a path ends up at that end state q_{E_i} and the IRIs PDF f_{E_i}. We use the mixture model to derive the final probability density function:

$$f_{\mathrm{final}}(x) = \sum_{i\in[0,N_L-1]} q_{E_i} f_{E_i}(x).$$

An example of this PDF is presented in FIG. 7(b).

Appendix C: Optimal Crescent Geometry

We repeat the parametric study in Section V for crescent DCPs. We use the same surface tension coefficients, α value, and numbers of large and small DCPs (N_S and N_L) in the calculation of R_C and V_R. We use the same numbers of DCPs because the results of Section IV C do not depend on the particle geometry. After we normalize $V_{\min} = 1$, the crescent DCPs have two parameters: θ and γ (FIG. 13). We obtain heatmaps for the lengths of the convergent ranges, R_C, and threshold system volumes V_R for these geometries in FIG. 12. We observe that geometries with a smaller θ have lower R_C and lower V_R. On the other hand, γ has a smaller effect on R_C and V_R, and lowering γ only lowers V_R. We observe that R_C and V_R are dominated by the value of θ. Here θ for spherical DCPs has an analogous role to h/r for cylindrical DCPs, in Section V. The value θ determines the relative water volume of the partial sphere.

The crescent DCP geometry that minimizes both the convergent range (R_C) and the system volume requirement (V_R) has a small opening and thin shell (FIG. 14(a)). While the best theoretical DCP has a small opening and thin shell, additional factors are involved in a physical DCP design. Authors of [7] show that a small opening makes it difficult for a DCP to load liquid. In addition, a thin shell is difficult to manufacture on the

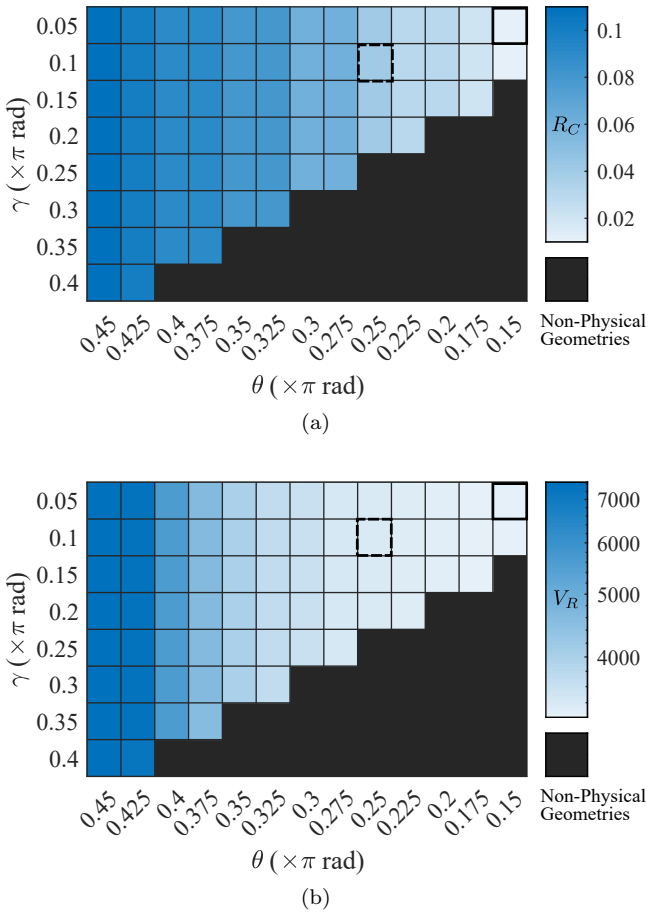

FIG. 12. The values of the optimization criteria for different crescent geometries, presented using heat maps. The theoretical optimal DCP geometry is represented by the box with a thick solid outline and the best DCP for physical experiments is marked by thick dashed outline. (a) Heat map representing R_C. DCPs that have smaller openings have lower R_C while the outer wall thickness of the DCP does not affect R_C. (b) Heat map (log scale) representing V_R. The DCP geometries with smaller openings and thicker walls have lower V_R, with the effect of wall thickness much smaller than the effect of opening size. The theoretical optimal DCP has $R_C = 0.01$ and $V_R = 3228$. The best DCP for physical experiments has $R_C = 0.04$ and $V_R = 3388$.

microscale. Taking the above factors into consideration, we can modify the parameters for an optimal crescent DCP that would fare well in physical experiments (FIG. 14(b)).

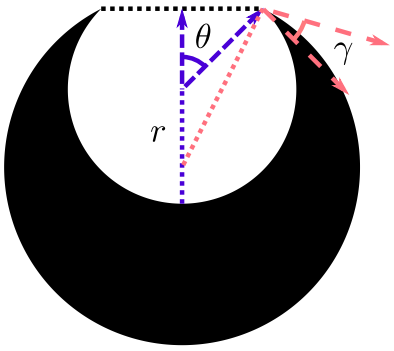

FIG. 13. Graphical representation of parameters r, θ, and γ for crescent geometries drawn over a 2D cross section of the crescent DCP. r is the radius of the inner sphere, θ is the angle between the vertical and the line connecting the inner center to the edge of the opening, and γ is the angle between the inner sphere and the outer sphere at the edge of the opening. The parameter angles are drawn with dashed arrows. Radii of the inner (blue) and outer sphere (red) are drawn as dotted lines.

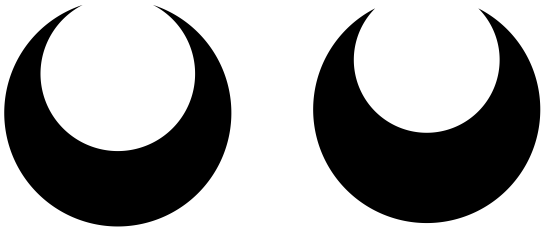

FIG. 14. Cross sectional representation for (a) the theoretical ideal DCP and (b) best DCP for physical experiments based on FIG. 12. The physical parameters of (a) are $\theta = 0.15\pi$ rad $\gamma = 0.05\pi$ rad. and for (b) are $\theta = 0.3\pi$ rad and $\gamma = 0.1\pi$ rad.

[1] N. R. Beer, B. J. Hindson, E. K. Wheeler, S. B. Hall, K. A. Rose, I. M. Kennedy, and B. W. Colston, On-chip, real-time, single-copy polymerase chain reaction in picoliter droplets, Analytical Chemistry **79**, 8471 (2007).

[2] H. E. Munoz, C. T. Riche, J. E. Kong, M. van Zee, O. B. Garner, A. Ozcan, and D. Di Carlo, Fractal lamp: Label-free analysis of fractal precipitate for digital loop-mediated isothermal nucleic acid amplification, ACS sensors **5**, 385 (2020).

[3] B. L. Wang, A. Ghaderi, H. Zhou, J. Agresti, D. A. Weitz, G. R. Fink, and G. Stephanopoulos, Microfluidic high-throughput culturing of single cells for selection based on extracellular metabolite production or consumption, Nature Biotechnology **32**, 473 (2014).

[4] D. Wang and S. Bodovitz, Single cell analysis: the new frontier in 'omics', Trends in Biotechnology **28**, 281 (2010).

[5] E. Z. Macosko, A. Basu, R. Satija, J. Nemesh, K. Shekhar, M. Goldman, I. Tirosh, A. R. Bialas, N. Kamitaki, E. M. Martersteck, J. J. Trombetta, D. A.

Weitz, J. R. Sanes, A. K. Shalek, A. Regev, and S. A. McCarroll, Highly parallel genome-wide expression profiling of individual cells using nanoliter droplets, Cell **161**, 1202 (2015).

[6] D. Mark, S. Haeberle, G. Roth, F. von Stetten, and R. Zengerle, Microfluidic lab-on-a-chip platforms: requirements, characteristics and applications, Chem. Soc. Rev. **39**, 1153 (2010).

[7] C.-Y. Wu, M. Ouyang, B. Wang, J. de Rutte, A. Joo, M. Jacobs, K. Ha, A. L. Bertozzi, and D. Di Carlo, Monodisperse drops templated by 3D-structured microparticles, Science Advances **6**, 10.1126/sciadv.abb9023 (2020).

[8] J. de Rutte, R. Dimatteo, M. van Zee, R. Damoiseaux, and D. Di Carlo, Massively parallel encapsulation of single cells with structured microparticles and secretion-based flow sorting, bioRxiv 10.1101/2020.03.09.984245 (2020).

[9] G. Destgeer, M. Ouyang, C.-Y. Wu, and D. Di Carlo, Fabrication of 3d concentric amphiphilic microparticles to form uniform nanoliter reaction volumes for amplified affinity assays, Lab on a Chip **20**, 3503 (2020).

[10] G. Destgeer, M. Ouyang, and D. Di Carlo, Engineering design of concentric amphiphilic microparticles for spontaneous formation of picoliter to nanoliter droplet volumes, Analytical Chemistry **93**, 2317 (2021).

[11] T. Vogel, Stability of a liquid drop trapped between two parallel planes, SIAM Journal on Applied Mathematics **47**, 516 (1987), https://doi.org/10.1137/0147034.

[12] T. Vogel, Stability of a liquid drop trapped between two parallel planes ii: General contact angles, SIAM Journal on Applied Mathematics **49**, 1009 (1989), https://doi.org/10.1137/0149061.

[13] A. D. Myshkis, V. G. Babskii, N. D. Kopachevskii, L. A. Slobozhanin, A. D. Tyuptsov, and R. Wadhwa, Low-gravity fluid mechanics, Translated from the Russian by Wadhwa, RS, XIX, 583 pp. 218 figs.. Springer-Verlag Berlin Heidelberg New York , 218 (1987).

[14] R. Gillette and D. Dyson, Stability of fluid interfaces of revolution between equal solid circular plates, The Chemical Engineering Journal **2**, 44 (1971).

[15] K. Ha, J. de Rutte, D. Di Carlo, and A. Bertozzi, Minimal surface configurations for axisymmetric microparticles, UCLA CAM report **20-38** (2020), ftp://ftp.math.ucla.edu/pub/camreport/cam20-38.pdf.

[16] G. McLachlan and D. Peel, *Finite Mixture Models*, Wiley Series in Probability and Statistics (Wiley, 2004).

[17] J. Bostwick and P. Steen, Stability of constrained capillary surfaces, Annual Review of Fluid Mechanics **47**, 539 (2015).

[18] M. Tjahjadi, H. A. Stone, and J. M. Ottino, Satellite and subsatellite formation in capillary breakup, Journal of Fluid Mechanics **243**, 297 (1992).

[19] P. Flajolet, D. Gardy, and L. Thimonier, Birthday paradox, coupon collectors, caching algorithms and self-organizing search, Discrete Applied Mathematics **39**, 216 (1992).

[20] R. L. Streit, The poisson point process, in *Poisson Point Processes: Imaging, Tracking, and Sensing* (Springer US, Boston, MA, 2010) pp. 11–55.